

Stability and sensitivity of interacting fermionic superfluids to quenched disorder

Jennifer Koch,^{1,2} Sian Barbosa,¹ Felix Lang,¹ and Artur Widera^{1,*}

¹*Department of Physics and Research Center OPTIMAS,*

RPTU Kaiserslautern-Landau, 67663 Kaiserslautern, Germany

²*TOPTICA Photonics AG, Lochhamer Schlag 19, 82166 Gräfelfing, Germany*

(Dated: September 10, 2024)

The microscopic pair structure of superfluids has profound consequences on their properties. Delocalized pairs are predicted to be less affected by static disorder than localized pairs. Ultracold gases allow tuning the pair size via interactions, where for resonant interaction superfluids shows largest critical velocity, i.e. stability against perturbations. The sensitivity of such fluids to strong, time-dependent disorder is less explored. Here, we investigate ultracold, interacting Fermi gases across various interaction regimes after rapid switching optical disorder potentials. We record the ability for quantum hydrodynamic expansion of the gas to quantify its long-range phase coherence. Contrary to static expectations, the Bose-Einstein condensate (BEC) exhibits significant resilience against disorder quenches, while the resonantly interacting Fermi gas permanently loses quantum hydrodynamics. Our findings suggest an additional absorption channel perturbing the resonantly interacting gas as pairs can be directly affected by the disorder quench.

INTRODUCTION

When an interacting system of fermionic particles is cooled below a critical temperature, bosonic pairs form, and the system becomes superfluid or, for charged fermions, superconducting. For ultracold Fermi gases, magnetic Feshbach resonances allow to modify the effective interaction strength [1] and thereby the underlying pairs from small, bound molecules to delocalized Cooper-type fermion pairs along the so-called crossover from a molecular Bose-Einstein condensate (BEC) to a Bardeen-Cooper-Schrieffer (BCS) superfluid [2, 3]. Between these two regimes, on resonance, a unitary Fermi gas (UFG) is realized exhibiting, for example, the largest superfluid critical velocity along the crossover [4, 5]. On resonance, the microscopic details of the gas are not relevant for the macroscopic properties [6], which has allowed to deduce universal properties highly relevant for nuclear matter, see for example [2, 3, 7–10]. The microscopic pairing has been investigated theoretically [11, 12] and experimentally using radio-frequency (rf) spectroscopy, for example, revealing different equilibrium properties such as the pair size or binding energy [13]. This microscopic pairing has profound consequences on the macroscopic quantum state. The excitation spectrum, for example, has been measured along the crossover in three-dimensional gases using Bragg spectroscopy [14, 15] and rf spectroscopy [16] and shows a clear change from a phononic-type branch in the BEC regime to a spectrum indicating dominant pair breaking in the BCS regime.

A prominent consequence of the pair nature in disordered potentials is summarized by the Anderson theorem [18], stating that delocalized Cooper pairs are only little affected by local perturbations, leading to only a moderate decrease of pairs for disordered systems due to a

disorder-induced reduction of the density of states close to the Fermi edge. Indeed, theoretical investigations of the BEC-BCS crossover in static disorder [19–23] show only a slight modification of the critical temperature in the BCS regime [19], together with a relatively small reduction of the order parameter and condensate fraction [20, 21], and an area of stability in the crossover region close to resonant interactions. Importantly, most studies have considered the weak disorder regime, and theoretical investigations of strong-disorder systems beyond perturbation theory are just emerging [24]. Experimentally, for strong interactions, the emergence of a fragmented Fermi gas has been observed in static disorder [25]. In our experiment, we consider the effect of strong and time dependent disorder.

By contrast, in the BEC regime, the critical temperature is more strongly suppressed by static disorder, together with order parameter and condensate fraction. Experimental transport measurements indicated a disorder-induced transition from a superfluid to a normal fluid in strong disorder [26]. The different behavior in the two regimes can be well explained by the fact that strong local interactions increase the ability of the superfluid to react to local perturbations, drawing the picture of the UFG being the most resilient superfluid. However, the specific properties of the pairs are expected to also modify the response of the superfluid to *time-dependent* disorder and determine how fast quantum properties decay for strong perturbation, or how fast they are recovered once the perturbation is absent. Experimental studies along the BEC-BCS crossover in the regime of static disorder regime are scarce, however, it has been shown, for example, the damping coefficient of dipole oscillations in a static disorder potential depends on the interaction strength [27].

In this work, we probe the response of ultracold, interacting Fermi gases of lithium atoms in the BEC-BCS crossover to strong perturbations in space and time via rapidly switched optical disorder potentials with focus on

* widera@physik.uni-kl.de

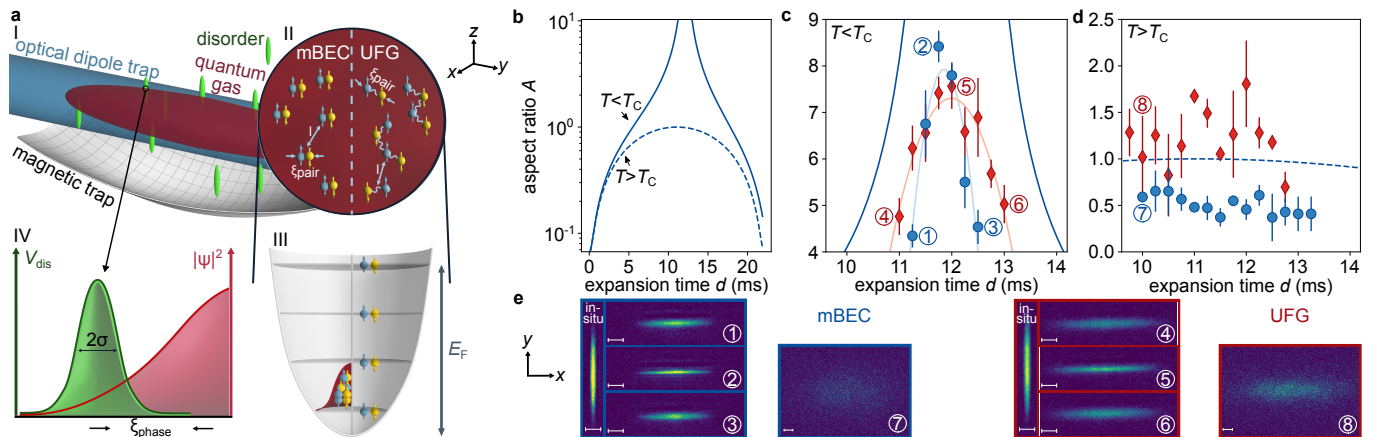


FIG. 1. **Experimental setup and method.** (a) (I) Schematic drawing of the experimental setup. The atomic cloud (red ellipsoid) is trapped in a combination of an optical dipole trap (blue cylinder) and a magnetic saddle potential (gray surface) and is superposed by the disorder field (green ellipsoids). (II) The microscopic pair size ξ_{pair} of an mBEC is much smaller than that of a UFG and the pair distance l equals roughly the pair size at resonance. (III) In the mBEC regime, the Feshbach molecules occupy the ground state of the harmonic trap and form a macroscopic wavefunction; by contrast in a UFG, the atoms occupy the levels according to the Pauli exclusion principle up to the Fermi energy E_F . (IV) The microscopically relevant length scale is the coherence (healing) length ξ_{phase} quantifying the length on which the system can respond as a macroscopic many-body wavefunction to perturbations such as disorder speckles. (b) Computed ideal time evolution of the aspect ratio for a degenerate gas (solid line) and a thermal gas (dashed line) for hydrodynamic expansion in our experimental traps without disorder, showing a divergence of the aspect ratio for a quantum fluid. For details see Methods. (c) Measured aspect ratio A of an mBEC at 763.6 G (blue circles) and a UFG at 832.2 G (red diamonds) as a function of the expansion time d around the maximum achievable value, which is limited by experimental details, see Ref. [17]. Each point is an average of four repetitions and the corresponding error bars show their standard deviations. The lines (light blue and light red) are guides to the eye. The solid dark blue line is equivalent to the computed ideal time evolution of the aspect ratio in (b) for a degenerate gas. (d) The same measurement as in (c) but for thermal gases. The dashed blue line is equivalent to the computed ideal time evolution of the aspect ratio in (b) for a thermal gas. (e) Absorption pictures for the measurement points indicated in panels (c) and (d), where the left most pictures show the initial quantum gases before expansion dynamics. The scales in the images mark a distance of 50 μm , also in the following figures.

the BEC side. We measure the time evolution of long-range coherence quantified via the ability of the gas to expand hydrodynamically. We find that, in marked contrast to the expectation of the static-disorder or weak-perturbation case, the quantum properties of a unitary Fermi gas are more strongly suppressed than a molecular BEC (mBEC), indicating an increased sensitivity. For quenches out of a disordered potential, we find that the UFG never restores quantum hydrodynamics for all parameters investigated, while an mBEC re-establishes quantum hydrodynamics, even when the quench leads to strong particle losses of up to 70%. Temperature measurements indicate an additional heating channel specific for gases close to resonant interactions, leading to strong local dephasing or pair breaking.

RESULTS

Experimental realization

We experimentally study the response of an ultracold gas of fermionic lithium-6 (Li) atoms prepared in the two lowest Zeeman substates (typically $N_i = 3 \cdot 10^5$ atoms per

spin state $i = \uparrow, \downarrow$) to fast switching of a disorder potential. The gas is prepared at a magnetic field of 763.6 G and has a temperature of $T \approx 200$ nK, corresponding to $T/T_F = 0.3$ in the BEC regime at 680 G. Typical values for trap frequencies are $\omega_x, \omega_y, \omega_z = 2\pi \times (345, 23, 220)$ Hz (see Methods). To tune the interaction between the two internal states, and hence the pair size of the superfluids formed, a broad Feshbach resonance at a magnetic field of 832.2 G is used [28]. In order to prepare a different interaction regime, we adiabatically ramp the magnetic field to the desired final value. Due to the ramp, the reduced temperature drops to values well below $T/T_F < 0.17$ at unitarity [29], implying $T < T_c$ with the critical temperature T_c [30]. This allows entering the different regimes of the BEC-BCS crossover, quantified via the interaction parameter $1/k_F a$, with the absolute value of the Fermi wave-vector

$$k_F = \sqrt{2mE_F}/\hbar \quad (1)$$

with the mass m of a Li atom and the Fermi energy [3]

$$E_F = \hbar\bar{\omega}(3N_{\uparrow\downarrow})^{1/3}, \quad (2)$$

the s -wave scattering length a , geometric mean $\bar{\omega}$ of the trap frequencies, and the total atom number $N_{\uparrow\downarrow}$ in

both spin states. The typical value for the Fermi energy is $E_F \approx k_B \times 670$ nK, with k_B the Boltzmann constant. Table I shows typical experimental parameters for the quantum gas at different magnetic fields.

Our observable revealing the response of quantum properties is the ability of the gas to undergo quantum hydrodynamic expansion. Expansion measurements probing hydrodynamic behavior have been used, for example, to characterize the transition between ballistic and hydrodynamic expansion [31] and to study the viscosity in a UFG [32]. Here, we employ hydrodynamic expansion as a measure of long-range phase coherence [17]. It allows us to time-resolve a quantum system's response to a strong perturbation in space and time, revealing the existence or reformation of a well-defined global phase. We can thus trace a genuine quantum property of a strongly interacting, three-dimensional many-body system subjected to strong and time-dependent perturbation. In a previous work [17], performed with the same experimental apparatus, we focused on investigations deep in the mBEC regime. Here, we extend this study by focussing on the markedly different stability and sensitivity of an mBEC compared to a UFG.

Hydrodynamics is initiated by suddenly switching off the optical dipole trap (see Fig. 1(a)), releasing the gas into a magnetic trap with a saddle potential configuration (confining in the x - y plane and anti-confining in z direction), where the change of aspect ratio A can be determined from absorption images. Here, the aspect ratio is defined as the ratio of the full width at half maximum (FWHM) of the 1D integrated column density distributions in x and y directions (see Fig. 1(a) and Supplementary Note 1A). The ensuing dynamics are markedly different for an ideal gas, a classical (thermal) interacting gas, or a quantum gas [33]. While an ideal gas shows a moderate change of aspect ratio due to single-particle dynamics in the trap, this change is enhanced by collisional hydrodynamics for repulsively interacting classical gases (see Fig. 1(b,d,e)). Quantum gases, however, show a remarkably large change in aspect ratio, as shown in Fig. 1(b,c,e). This strong increase beyond classical collisional hydrodynamics is tightly connected to the existence of a well-defined global phase, i.e., long-range phase coherence [17]. We note that a comparable quantum enhancement cannot be observed for the BCS side of the resonance, i.e., negative interaction parameters $1/k_F a < 0$ even close to resonance, in agreement with previous observations of the vanishing of hydrodynamics when approaching the BCS regime [34]. We attribute this to breaking of the underlying fermionic pairs due to the strongly reduced density and hence pairing gap during the expansion. Our analysis is therefore restricted to positive interaction parameters $1/k_F a > 0$ which will be the focus throughout the remainder of this work. For more details of the experimental setup, see Methods and Ref. [35].

The perturbation of the system is controlled through a repulsive optical speckle disorder-potential with mean potential strength \bar{V}_{dis} and correlation lengths of $\sigma_{x,y} = 750$ nm and $\sigma_z = 10$ μ m, see Fig. 1(a). Here, the correlation length is defined as the $1/e$ -width of the speckle pattern's autocorrelation function and quantifies the typical grain size [17]. The mean potential strength is of the order of the superfluid's chemical potential μ ($\mu_{\text{BEC}} = k_B \times 390$ nK for an mBEC and $\mu_{\text{UFG}} = k_B \times 480$ nK for a UFG) and the short correlation length is larger but of the order of the quantum gases' coherence or healing length ξ ($\xi_{\text{heal}} \approx 230$ nm for $1/k_F a \approx 1$). Thus, the static perturbation is strong. Since the polarizability of a Feshbach molecule is twice the value for a single atom, the potential height of the speckle potential is twice that of the molecules compared to the unbound atoms for the same laser power [36, 37]. In tunneling experiments along the BEC-BCS crossover, for example, this does not seem to play a role, and the dynamics for constant optical potentials along the crossover could be compared [38, 39]. Measurements for atom losses after disorder quenches (see Supplementary Note 1B) show, however, that the loss curves collapse to a single curve, when the disorder laser power for the UFG is twice the power for an mBEC, supporting our assumption of different potentials $V^{(\text{mBEC})} \approx 2V^{(\text{UFG})}$ for the same laser power. This observation indicates that the disorder locally affects molecules in the mBEC and atoms in the UFG. In the following, the disorder is given in laser power of the disorder, providing comparison of potential heights differing by a factor of two. Moreover, the disorder potential can be either ramped adiabatically with respect to h/μ or be quickly switched on or off with switching times being shorter than h/μ (see insets of Figs. 2a) and 3a)), so that the many-body system cannot adiabatically follow the dynamics. The speckle realization is changed after each measurement. Furthermore, for our parameters, classical trapping cannot occur, because the mobility edge is close to the classical percolation threshold in our system [36, 40]. For a detailed description and characterization of the disorder potential see Methods and [24, 41, 42].

Decay of quantum hydrodynamics

We first study the impact of a suddenly applied disorder potential on a superfluid in different interaction regimes. We thus analyze the collapse of the hydrodynamic expansion after a sudden quench into the disorder potential of variable duration τ_{on} . In addition to studying the hydrodynamic behavior, we have additionally examined the density response for all measurements along the crossover shown in the following and report it in the Supplementary Note 2. In Fig. 2(a), we compare the decay of the maximum achievable aspect ratio of

TABLE I. Typical characteristic parameters of the quantum gas for three specific magnetic field values. We extract the values of the s -wave scattering length a from [28] and they are given in units of the Bohr radius a_0 . The wave vector is computed according to Eq. 1 with the Fermi energy eq. (2). The densities n_0 given are peak densities in the center of the trap.

magnetic field B (G)	s -wave scattering length a (a_0)	Fermi wave vector k_F (μm^{-1})	peak density n_0 (10^{12}cm^{-3})
680.0	1238	4.02	11.3
763.6	4509	4.06	5.3
832.2	1758077	4.09	3.8

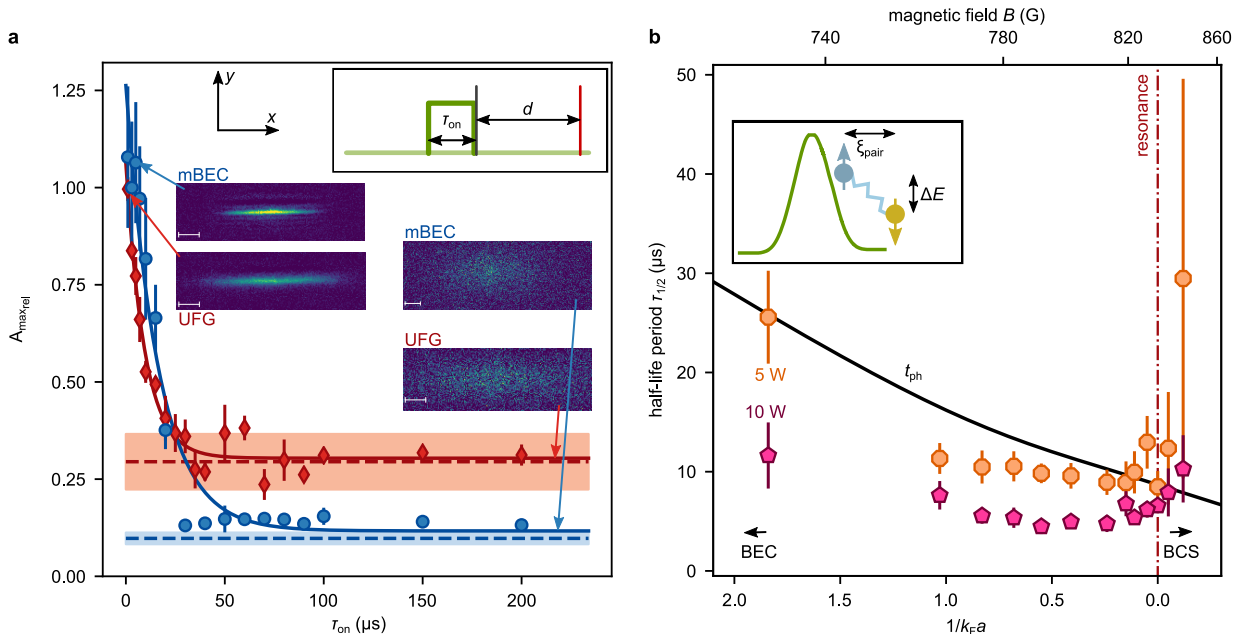


FIG. 2. **Decay of quantum hydrodynamics.** (a) Decay of the relative maximum aspect ratio $A_{\text{max,rel}}$ (normalized to the maximum aspect ratio without disorder) as a function of the disorder-pulse duration τ_{on} for an mBEC at 763.6 G ($1/k_F a = 1.04$, blue circles) and a UFG ($1/k_F a = 0$, red diamonds). The blue (red) dashed lines show independently measured aspect ratios for classical hydrodynamics in thermal gases at 763.6 G (832.2 G), i.e. including collisional hydrodynamics, and its uncertainty as shaded areas (for more details see Supplementary Note 1C). The red and blue lines are exponential-decay fits to the data. Insets show the experimental sequence of disorder quench pulse (green), and subsequent expansion time d and imaging (red vertical line) as well as absorption pictures of the two regimes for a short and long disorder pulse. (b) Half-life period $\tau_{1/2}$ as a function of interaction parameter in the crossover for 5 W (orange octagons) and 10 W (pink pentagons) disorder laser power. In the crossover, the ability for hydrodynamic expansion decays significantly faster compared to interaction parameters $1/k_F a > 1$ far from the crossover [17]. The black line shows the calculated dephasing time $t_{\text{ph}} = \hbar/\Delta E = \hbar\sigma_{x,y}/(\bar{V}_{\text{dis}}\xi_{\text{pair}})$ of the two atoms with opposite spin for $2\bar{V}_{\text{dis}}$ for molecules (disorder laser power of 10 W). At this time scale, two paired atoms acquire a phase difference of unity in the disorder potential gradient, see inset sketch. Here, ξ_{pair} is taken from the calculation in Fig. 4(b).

hydrodynamic expansion of an mBEC ($1/k_F a = 1.04$) and a UFG at resonance ($1/k_F a = 0$) below the critical temperature as a function of τ_{on} . All data are normalized to the maximum aspect ratio change experimentally obtained without disorder, see Fig. 1(c). Here, for the mBEC regime, the speckle laser power is set to 5 W, corresponding to $\bar{V}_{\text{dis}}^{\text{mBEC}}/\mu_{\text{mBEC}} \approx 1.6$ and 10 W for the UFG $\bar{V}_{\text{dis}}^{\text{UFG}}/\mu_{\text{UFG}} \approx 1.3$, ensuring approximately the same, strong disorder potential height in the two regimes. As seen in Fig. 2(a), the maximum aspect ratio decreases after suddenly applying the disorder potential for a certain time τ_{on} approximately exponentially, indicating a collapse of quantum hydrodynamics and

hence long-range coherence. The minimum aspect ratio reached in steady state corresponds to the respective aspect ratio of a thermal gas in the mBEC regime or at resonance. We find that the UFG stabilizes at a higher value of the aspect ratio compared to the mBEC, which we attribute to higher interaction strength and hence stronger classical hydrodynamics in this regime. As shown in the Methods, the change of aspect ratio depends on the trap frequencies rather than potential depth. Therefore, the difference in classical hydrodynamics cannot be due to the different mass of molecules compared to atoms. The half-life period $\tau_{1/2}$, i.e., the time at which the aspect ratio has collapsed to half of

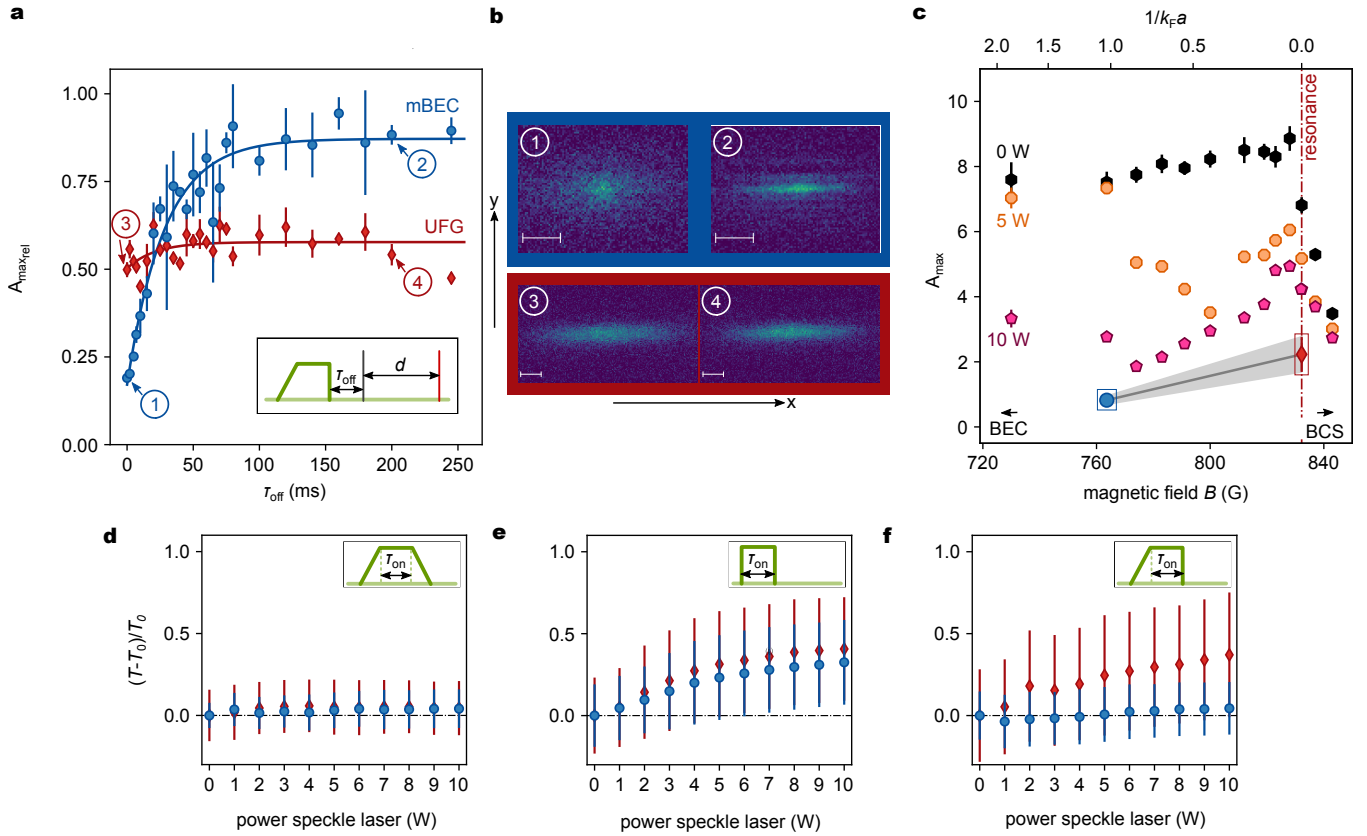


FIG. 3. Revival of quantum hydrodynamics. (a) Relative revival of the maximum aspect ratio (normalized to the maximum aspect ratio without disorder) $A_{\max, \text{rel}}$ as a function of the revival time τ_{off} in the mBEC regime (blue circles) and in the UFG (red diamonds). The red and blue lines are exponential fits. The inset shows the timing sequence. For the unitary (mBEC) regime, a speckle laser power of 10 W (5 W) is used to approach identical disorder potentials. (b) Absorption pictures for the measurement points indicated in panel (a). (c) Maximum absolute aspect ratio A_{\max} after quenching out of disorder as a function of the interaction parameter $1/k_F a$. Dots are measurements for 5 W (orange octagons), 10 W (purple pentagons), and for 0 W (black hexagons) disorder laser power. Each data point is an average of the three largest aspect ratios during the expansion, its uncertainty is the standard deviation of these three points. The blue (mBEC) and red (UFG) data points, marked with a rectangular box, indicate the independently measured aspect ratios of a thermal gas. The gray line is a guide to the eye between the two points including its uncertainty. (d-f) Measured relative temperature increase for different disorder quench protocols shown in the insets, as a function of disorder power when applied to an mBEC (blue circles) or a UFG (red diamonds). The pulse duration is set to $\tau_{\text{on}} = 100$ ms. Each data point is an average of five repetitions and their standard deviation is indicated as error bar.

the initial value, of the UFG is shorter with $(7 \pm 1) \mu\text{s}$ than for the mBEC with $(11 \pm 2) \mu\text{s}$.

From studies in the mBEC regime [17], a relatively constant $\tau_{1/2}$ value was found for a broad range of interaction parameters outside the crossover $1/k_F a > 1$. The underlying mechanism explaining the time scales and numerical simulations of the phase evolution suggested imprinting of a random local phase onto the mBEC by the disorder. The resulting local phase evolution destroys long-range phase coherence, and for a broad range of interaction strengths, it is only dependent on the properties of the disorder potential but not on interaction properties. In Fig. 2(b), we show the $\tau_{1/2}$ values when entering the crossover. The clearly faster decay of long-range phase coherence indicates that the decay now does depend on interaction, in contrast to

deep in the weakly interacting BEC regime ($1/k_F a \gg 1$). Hence, an additional mechanism suppressing long-range phase coherence is present in the crossover. To illustrate this, we compare the half-life period with a heuristic dephasing time $t_{\text{ph}} = \hbar/\Delta E$, which describes the time it takes for the two-particle wave function of the pair to accumulate a phase shift of unity due to a potential difference ΔE in the disorder field. A Feshbach molecule experiences a reduced potential difference compared to a more delocalized Cooper pair due to its smaller spatial extension. The decay of the half-life period by entering the crossover shows a qualitative similar behavior as the decrease of the dephasing time, illustrating that a microscopic mechanism perturbing the pair structure could become relevant in the crossover.

Revival of quantum hydrodynamics

Complementary, we study the revival of the long-range phase coherence when the system is quenched out of a disordered potential. Experimentally, we adiabatically ramp up the speckle potential in a 50 ms linear ramp to avoid excitations in the cloud. The potential is held for 100 ms before suddenly switching off the disorder, see inset in Fig. 3(a). After a varying hold time τ_{off} without disorder, the cloud is expanded for a time d into the magnetic saddle potential to allow for hydrodynamic expansion before imaging. The two regimes of mBEC and UFG show a strikingly different behavior, illustrated in Fig. 3(a,b). While the long-range phase coherence for the mBEC recovers completely with an exponential time constant $\tau_{1/2}^{\text{off}} = (20 \pm 3)$ ms, the UFG does not fully revive. We show the maximum achievable value of the aspect ratio in Fig. 3(c) along the crossover without disorder and for two different disorder laser powers. Without disorder, we find a maximum aspect ratio that slightly increases for decreasing interaction parameter $1/k_{\text{F}}a$ in the crossover, until it rapidly decays for negative scattering length, i.e., on the BCS side of the crossover $1/k_{\text{F}}a < 0$. For strongest disorder applied, the gas quenched out of disorder behaves similar to a classical gas for all interaction strengths. An interesting behavior is observed for intermediate disorder laser powers. Here, the gas can fully revive in the mBEC regime, which is consistent with previous studies [17]. For decreasing interaction parameter $1 > 1/(k_{\text{F}}a) > 0.5$, the maximum aspect ratio decays and approaches the classical limit until it increases again for $0.5 > 1/(k_{\text{F}}a) > 0$. However, for all interaction strengths in the crossover, quantum hydrodynamics does not revive, in stark contrast to the mBEC regime outside the crossover. This is even more remarkable, since for the equilibrium, weak-disorder phase diagram, the critical temperature in the mBEC regime is expected to be more strongly reduced with disorder compared to the UFG [19, 43].

In order to characterize the many-body state after the quench, we additionally measure the temperature increase for different disorder ramp procedures, see Methods. In Fig. 3(d-f), we show the relative temperature increase for the limiting cases of an mBEC and a UFG for a fully adiabatic ramp, a disorder pulse (as used in Fig. 2), and rapid quench out of disorder (as used in Fig. 3(a,c)).

For the fully adiabatic ramp (Fig. 3(d)), neither mBEC nor UFG show a significant increase of temperature. For a quench pulse, i.e. a quench into and a quench out-of the disorder (Fig. 3(e)), both gases are significantly heated and show a similar increase in temperature. While the relatively large error bars do not allow to identify the speckle power when the gas is heated above the critical temperature, for the highest disorder potential the UFG shows $T > T_c$. Interestingly, for an adiabatic loading into

the disorder potential and a subsequent quench out of disorder, Fig. 3(f), the UFG is heated more strongly than the mBEC, where for a speckle laser power of 10 W the UFG is brought above the critical temperature, while the mBEC is mainly unaffected. The maximum thermal energy increase in Fig. 3(f) for the UFG is $\Delta E/E_{\text{F}} \approx 0.09$, which may be compared to the energy needed for pair breaking $2\Delta_{\text{gap}} = 1.8E_{\text{F}}$ [44]. The energy absorbed by the UFG from the quench thus brings the gas close to or above the critical temperature, and quantum hydrodynamic expansion breaks down.

In order to check if the temperature increase is the main reason for collapse of quantum hydrodynamics, we study disorder quenches in an open system, where high-energetic particles can escape from the trap effectively reducing the mean energy. This is achieved by reducing the depth of the optical dipole trap, allowing a certain fraction of atoms with highest energy to escape. The relation between the fraction of particles lost and the potential depth is shown in the Supplementary Note 3. We find that, even for losses of more than 60%, the mBEC recondenses and shows a close-to-full revival of hydrodynamic expansion, and hence long-range coherence. By contrast, the UFG does not show a significant increase in quantum hydrodynamics for any particle loss.

DISCUSSION

Our data presented suggests that even for a UFG initially adiabatically prepared to populate the ground state of a disorder potential, a quench out of disorder permanently destroys long-range quantum coherence. This is in stark contrast to the equilibrium expectation, where a UFG has so far been found to form a superfluid showing largest critical velocity. The temperature measurements suggest the appearance of an additional absorption channel for the UFG, which is not present for the mBEC. This additional heating brings the UFG close to or above the critical point, and quantum hydrodynamic ceases.

A first intuitive understanding of the microscopic origin of this heating channel can be obtained by considering the microscopic pairing structure along the BEC-BCS crossover [11, 45–47]. Figure 4(a) compares relevant energies of the quenched disorder potential with energy scales of the many-body system, especially the many-body gap $2\Delta_{\text{gap}}$ and the molecular binding energy $E_{\text{B}} = \hbar^2/(ma^2)$ [34], in the BEC-BCS crossover. Calculations are done using experimental parameters, specifically total atom number $N_{\uparrow\downarrow} = 5.13 \times 10^5$ (average of experimental values) and trap frequencies $\omega_x, \omega_y, \omega_z = 2\pi \times (345, 23, 220)$ Hz. The Fermi energy is calculated according to eq. (2). Besides, the mean disorder potential strength \bar{V}_{dis} is shown and the correlation energy $E_{\sigma} = \hbar^2/(m\sigma^2)$ [48] is calculated. These two quantities are different for atoms or molecules at the same laser power due to the difference in mass. The energy scale of the quench time of the

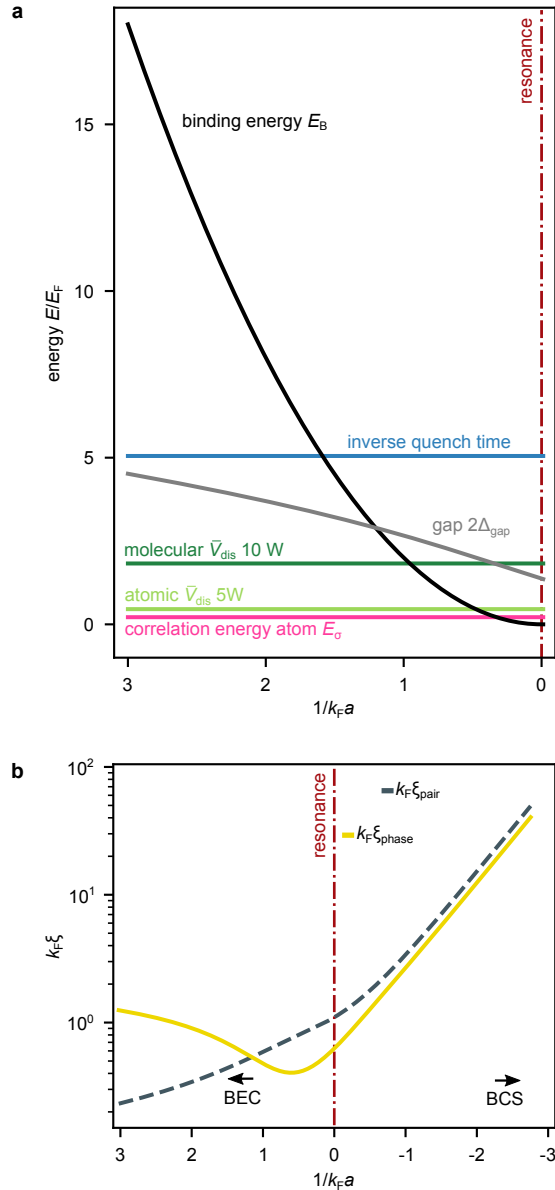


FIG. 4. **Energy and length scales.** (a) Comparison of relevant energy scales along the crossover in units of the Fermi energy E_F as a function of the interaction parameter $1/k_F a$. Binding energy and gap are calculated for the three-dimensional case at zero temperature according to Refs.[11, 45–47]. Calculations of the further energies are done with experimental parameters. (b) Pair correlation length ξ_{pair} (gray dashed line) and phase coherence length ξ_{phase} (yellow line) as a function of the interaction parameter $1/k_F a$, calculated for the three-dimensional case at zero temperature according to Refs.[11, 45–47].

speckle field is given by $E_{\text{quench}} = \hbar/t_{\text{on}}$, where the time to switch on the speckle field instantaneously is measured with $t_{\text{on}} = 2.26 \mu\text{s}$.

Figure 4(b) shows the change of coherence lengths ξ_{pair} and ξ_{phase} of the interacting many-body system along the BEC-BCS crossover, see Refs. [11, 45–47]. Deep in the

mBEC regime, both differ significantly. The molecules are relatively small and the healing length $\xi = \xi_{\text{phase}}$ is much larger, increasing for larger interaction parameters $1/(k_F a)$. Hence, $\xi_{\text{phase}} > \xi_{\text{pair}}$. Approaching the resonance, the healing length decreases, while the molecules become larger as the molecular bound state energy approaches the dissociation threshold. Upon entering the crossover $1/(k_F a) \approx 1$, the two length scales approximately coincide $\xi_{\text{phase}} = \xi_{\text{pair}}$. On resonance, the pair coherence length is larger than the phase coherence length. In the BCS regime, the two quantities scale the same and differ only by some constant factor. The coherence lengths allow estimating the effect of local potential changes onto the fermionic pair.

Comparing these scales with energy and length scales of the quenched disorder potential, we find that, first, deep in the mBEC regime, the pair size is much smaller than any length scale of the disorder potential. At the same time, the molecular binding energy is so large that no energy scale of the disorder is comparable. Thus, the disorder potential primarily affects the global wave function, which is perturbed at the length scale of the healing length and the energy scale of the chemical potential, leading to wave-like excitations of the many-body system. In the crossover, however, the pair size increases and becomes of the order of the healing length, being smaller but of the order of the correlation length of the disorder, where the UFG shows the largest pair size of the order of $1/k_F$. As shown in the inset of Fig. 2(b), local gradients of the disorder hence become relevant on the length scale of the pair. At the same time, the many-body gap as well as the binding energy of the molecular state decreases when approaching the resonance $1/k_F a \rightarrow 0$. Here, the energy scales of the time-dependent disorder, specifically the inverse ramping time $E_{\text{quench}} = \hbar/t_{\text{on}}$, but also the correlation energy $E_\sigma = \hbar^2/(m\sigma^2)$ [48] or mean potential strength \bar{V}_{dis} , become compatible to or larger than the many-body gap or the binding energy $E_B = \hbar^2/(ma^2)$ [34] for sufficiently strong interaction. Hence, pair breaking can occur.

This microscopic matching of pair properties to the length and energy scales of the quenched disorder can explain the additional absorption channel for energy in the UFG. It brings the many-body system close to or even above the critical temperature, where quantum dynamics cease. For two-dimensional strongly disordered superconductors it was shown in Ref. [49] that the strongly disordered many-body system can form superconducting islands separated by an insulating sea, where the islands are not phase coherent. A fragmented Fermi gas, comprising unconnected islands of bound pairs, in strong disorder was proposed in Ref. [25] to explain the experimentally observed density modulations. Our system is three dimensional, and our disorder is formed by a repulsive potential far from the percolation threshold, so that the system is expected to be always fully connected. However, our observation might point toward a local dephasing of the UFG by strong disorder

quenches, potentially at the level of individual pairs. It will be interesting in the future to see if the UFG quenched out of strong disorder might contain islands of Fermi pairs that connect to a smooth density, but preserve phase difference that prevent global quantum hydrodynamic expansion.

Our studies of the stability of interacting Fermi superfluids along the BEC-BCS crossover in the presence of a strong time-dependent perturbation clearly show that the static properties of the disordered BEC-BCS crossover are very different from the observations obtained in this work for the time-dependent nonequilibrium case. In the future, it will be interesting quantitatively map out the phase diagram of the disordered BEC-BCS crossover away from equilibrium. Additionally, reducing the dimensionality of the gas and producing homogeneous gases in different dimensions will provide a deeper and more quantitative insight into the connection between microscopic pairing mechanism and macroscopic nonequilibrium dynamics.

METHODS

Quantum-gas preparation

We evaporate our laser-cooled samples at a magnetic field of 763.6 G ($a = 4509a_0$, with the Bohr radius a_0) in the BEC regime for all observed interacting regimes. During evaporation, the laser power of the optical-dipole trap (ODT) is lowered from 140 mW to 8 mW by two subsequent exponential power ramps during 4.38 s. This final laser power of 8 mW is relatively low and enables controlling atom losses through disorder quenches. After the evaporation step, the laser power is held for 250 ms to equilibrate the temperature of the cloud. Subsequently, the trap is compressed by increasing the optical-dipole-trap (ODT) laser power up to 80 mW during 300 ms. By varying the level of compression, the amount of losses due to the disorder field can be adjusted. No losses occur at a power of 80 mW.

After the condensate is formed, the magnetic field is adiabatically ramped to the desired field for interaction control during 200 ms. The cloud is trapped in a combination of the ODT, created with a focused laser beam of a wavelength of 1070 nm and a magnetic saddle potential. Further, the magnetic field strength determines the scattering length and, therefore, the interacting regime between the two spin states.

Before disturbing the cloud by quenching the disorder field, another holding time of 30 ms ensures that no excitations of the cloud are present after changing the magnetic field strength. The trap frequencies in the radial directions, x and z , increase with the square root of the laser power of the ODT. The axial trap frequency, y direction, is within the range used, independent of the laser power. Changing the magnetic field has a

negligible influence on the trap frequency compared to the genuine frequency. The trap frequencies are $\omega_x, \omega_y, \omega_z = 2\pi \times (345, 23, 220)$ Hz for an ODT laser power of 80 mW and a magnetic field strength of 763.6 G.

Disorder potential

A far-off resonant, blue-detuned laser with a wavelength of 532 nm generates the potential. The envelope of the laser is a Gaussian with waists of (466 ± 25) μm and (414 ± 25) μm along two orthogonal directions [50]. Moreover, the optical speckle potential is formed by shining the collimated laser beam through two successive speckle plates. An objective focuses the random phase pattern on the position of the atoms. Hence, anisotropic speckle grains with sizes $\sigma_{x,y} = 750$ nm and $\sigma_z = 10$ μm are formed. The speckle plates are mounted in a motorized turntable; one of them is rotated by a certain angle after each measurement, so that the interference potential changes in each experimental realization. We characterize the strength of the disorder potential V_{dis} by the mean disorder potential \bar{V}_{dis} , which is the overall spatial average. For comparison, we may express the mean disorder potential in units of the unperturbed chemical potential. For the mBEC, the chemical potential [51]

$$\mu_{\text{mBEC}} = \frac{\hbar\bar{\omega}}{2} \left(\frac{15 \frac{N_{\uparrow\downarrow}}{2} a_{\text{dd}}}{a_{\text{ho}}} \right)^{2/5} \quad (3)$$

is established through the Gross-Pitaevskii equation, where $a_{\text{dd}} = 0.6a$ [52] is the s -wave scattering length for molecules, $a_{\text{ho}} = \sqrt{\hbar/(2m\bar{\omega})}$ the harmonic oscillator length with the mass m of the lithium atom. The chemical potential of the UFG [53]

$$\mu_{\text{UFG}} = \sqrt{1 + \beta} E_{\text{F}} \quad (4)$$

is proportional to the Fermi energy with the universal constant $\sqrt{1 + \beta}$.

Dependence of the expansion dynamics on interactions

An mBEC and a UFG show quantum hydrodynamic expansion [34]. In the case of an mBEC, a UFG, or a thermal gas, the in-situ aspect ratio is independent of the mass of the particles. The radii for all three cases individually depend on the mass, but it cancels when computing the aspect ratio. Instead, the aspect ratio depends on the trap frequencies. During expansion, the aspect ratio $\frac{R_x(t)}{R_y(t)} = \frac{b_x(t) \omega_y}{b_y(t) \omega_x}$ changes according to scaling factors b_i

$$\ddot{b}_i - \frac{\omega_i^2}{b_i (b_x b_y b_z)^\gamma} = 0, \quad (5)$$

which can be derived from the Euler equation [34]. The scaling factors are independent of the mass. The expansion of the mBEC and the UFG differ by the exponent γ (BEC $\gamma = 1$, UFG $\gamma = 2/3$), since the difference of the chemical potential depends on the density in the two regimes ($\mu_{\text{BEC}} \propto n$, $\mu_{\text{UFG}} \propto n^{2/3}$) [54]. Moreover, the trap frequencies are identical for a Feshbach molecule or a single atom, and hence the aspect ratio during expansion is independent of the mass of the particles. A thermal gas shows a ballistic expansion with scaling factors also independent of the particle mass.

Determination of the half-life period by expansion dynamics

For the decay and the revival of the long-range phase coherence (where the cloud fully recovers), the half-life period $\tau_{1/2}$ is determined similar to Ref. [17]. When plotting the aspect ratio as a function of the speckle-pulse length τ_{on} or the revival time τ_{off} , it shows an exponential evolution to a steady state.

This behavior is fitted with an exponential decay function (see Fig. 2(a) and 3(a))

$$h(\tau) = a e^{-\gamma\tau} + o, \quad (6)$$

with γ is the decay constant and, o and a are further fit values. Here, the half-life period is calculated via

$$\tau_{1/2} = \ln(2)/\gamma. \quad (7)$$

The uncertainty of the half-life period is taken as the fit uncertainty.

Temperature measurements

We have measured the relative temperature increase in the quantum gases for an mBEC at 763.6 G and a UFG at 832.2 G through the disorder potential for different disorder ramp procedures (see Fig. 3(d-f)) applying up to 10 W laser power creating the disorder field. As a reference, we measure the gas temperature T_0 without the disorder field. Three disorder ramping procedures are investigated. First (Fig. 3(d)), the disorder field is adiabatically introduced by a linear ramp during a 50 ms, held for 100 ms, and subsequently switched off in 50 ms by a linear ramp. Second (Fig. 3(e)), the disorder is rapidly switched on (switching time of $t_{\text{on}} = 2.26 \mu\text{s}$) for a rectangular pulse for a duration of duration $\tau_{\text{on}} = 100$ ms. Lastly (Fig. 3(f)), the disorder field is adiabatically introduced by a linear ramp during a 50 ms, and subsequently the power is held for 100 ms, before the field is suddenly switched off. After a holding time of 100 ms, the magnetic field is adiabatically swept to 680 G. Subsequently, the cloud is imaged in situ via absorption imaging. At this magnetic field strength, a bimodal fit to the density profiles allows the extraction

of the temperature of the cloud.

DATA AVAILABILITY

All data of the figures in the manuscript are available in a Zenodo repository, Ref. [55], DOI:10.5281/zenodo.13292670.

ACKNOWLEDGMENTS

We thank Carlos A. R. Sá de Melo, Henning Moritz, Giuliano Orso, Giacomo Roati, Wilhelm Zwerger, Benjamin Nagler, and Alexander Guthmann for helpful discussions and Eloisa Cuestas for carefully reading the manuscript. This work was supported by the German Research Foundation (DFG) via the Collaborative Research Center Sonderforschungsbereich SFB/TR185 (Project 277625399). J.K. was supported by the Max Planck Graduate Center with the Johannes Gutenberg-Universität Mainz. We acknowledge help by Valeriya Mikhaylova with the graphical implementation of Fig. 1a).

AUTHOR CONTRIBUTIONS

A.W. conceived and supervised the research. J.K. took and analyzed the experimental data, and calculated the theoretical estimations. S.B. and F.L. helped in running the experimental apparatus and taking data. All authors contributed to the interpretation of the data, writing of the manuscript and critical feedback.

COMPETING INTERESTS

The authors declare no competing interests.

SUPPLEMENTARY MATERIAL FOR STABILITY AND SENSITIVITY OF INTERACTING FERMIONIC SUPERFLUIDS TO QUENCHED DISORDER

In this supplemental material, we present further details on the experimental setup and methods (see Supplementary Note 1) and provide additional information on the density response to disorder quenches (see Supplementary Note 2) and open-system disorder quenches (see Supplementary Note 3).

SUPPLEMENTARY NOTE 1: DETAILS ON THE EXPERIMENTAL SETUP AND METHODS.

A. Extraction of the maximum aspect ratio

The aspect ratio is the ratio of the width of the clouds in the axial and radial directions, where the width is extracted from the absorption images. We integrate the density distributions in the imaging plane separately along the x and y directions to obtain two one-dimensional density profiles. The width of the cloud is determined as the fitting parameter of the 1D density profile for each direction. However, the density profiles of an mBEC and a UFG are generally different, and the Thomas-Fermi density profiles of an mBEC and a UFG do not have the same exponent. To avoid any method-depending systematics and to obtain a homogeneous evaluation method when analyzing the density profiles along the crossover, we employ the same fitting profile for all density distributions measured at various interaction parameters. This is supported by Supplementary Fig. 1, where the different fitting functions are compared and show only small differences. Thus, we take the profiles that are suitable for a BEC as fit functions for the whole crossover. After expansion, the radial direction is the long axis of the cloud through inversion of the aspect ratio.

In the x direction, we apply a 1D Thomas-Fermi profile n_{TF} [56]

$$n_{\text{TF}} \propto \left(1 - \frac{i^2}{r_{\text{TF}_i}^2}\right)^2, \quad (\text{S1})$$

with r_{TF_i} the radius in i -direction. Besides that, in the y direction, the density shows a sharp peak and a non-neglecting background, which makes it difficult to fit a Thomas-Fermi profile. Therefore, this direction is fitted with a 1D-bimodal fit $n_{\text{bimodal}} = n_{\text{G}} + n_{\text{TF}}$. The background is fitted with a Gaussian 1D-profile n_{G} given by

$$n_{\text{G}} \propto e^{-\frac{i^2}{2s_{i\text{G}}^2}}, \quad (\text{S2})$$

with the width $s_{i\text{G}}$. We extract the full width at half maximum (FWHM) of the total fitted 1D-density profiles for both directions. The aspect ratio is the ratio of the FWHM of the x direction by the one of the y direction. By varying the expansion time d , we measure a change in the aspect ratio. The maximum value quoted in the main text is extracted as the mean from the three highest ratios during the expansion evolution, and their standard deviation is indicated by the error bars.

For comparison, on resonance, the 1D Thomas-Fermi density profile n_{TFU} is [57]

$$n_{\text{TFU}} \propto \left(1 - \frac{i^2}{r_{\text{TFU}_i}^2}\right)^{5/2}, \quad (\text{S3})$$

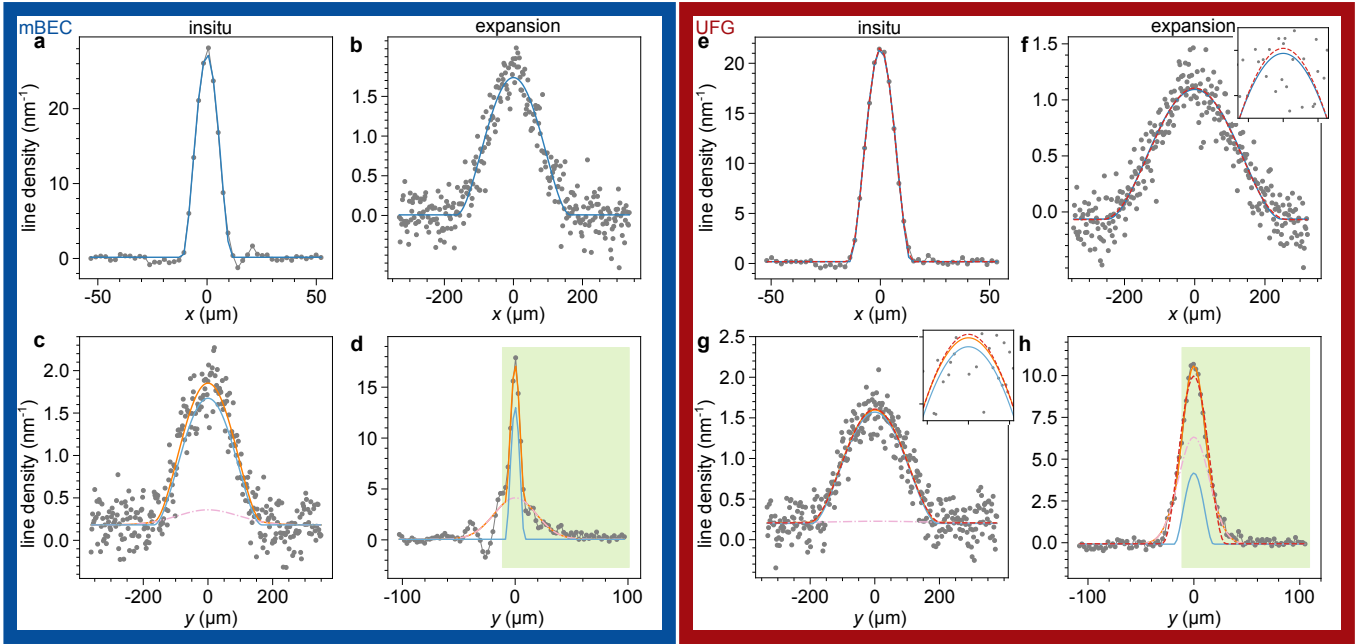
with the radius r_{TFU_i} in i -direction. Supplementary Figure 1 shows fits of the measured density profiles and compares a bimodal fit (Eq. S1 & S2) with the Thomas-Fermi

fit on resonance (Eq. S3) for clouds at resonance. Both versions fit the data well.

B. Measuring particle losses versus trap depth

We adjust the atom losses induced by the disorder field through different compression values of the trap. A lower ODT laser power leads to a smaller compression and a lower trap depth, which leads to larger atom losses in a disorder quench and vice versa. For a sufficiently large compression of the trap, we measure no atomic losses that are caused by the speckle field. Supplementary Figure 2 shows the mapping between the power of the ODT laser after compression and the remaining particles in the trap. The measurements are performed for the mBEC regime at 763.6 G and on resonance at 832.2 G. As noted in the main text, the disorder strength of the speckle potential is twice as much for molecules compared to single atoms for the same laser power. Hence, for the mBEC regime, the speckle-laser power is set to 5 W and for the unitary regime to 10 W to get the same effective disorder potential. As a reference, the atom number is also measured without a disorder field for both regimes. For an identical trap depth, the remaining particles in the trap are equal in both regimes. In addition, we have investigated the losses for two different instantaneous disorder quenches, one when switching the disorder field on and one when switching it off. The amount of atoms that leave the trap is higher for a quench into the disorder field compared to a quench out of the disorder field, where we introduce the speckle potential adiabatically rather than instantaneously (see Supplementary Fig. 2). Moreover, we have measured similar loss curves for the other magnetic field strengths used. No losses occur for all applied magnetic fields for an ODT laser power of 80 mW.

For these measurements, as for the measurements presented in the main text, the evaporation of the cloud takes place at 763.6 G, and the power of the ODT laser is lowered to 8 mW. Subsequently, the cloud is held for 250 ms before the trap is compressed. The power of the ODT laser and hence the trap compression is set to a selected value. As the next step, the magnetic field is ramped to the desired value in a duration of 200 ms. Subsequently, the cloud is held in the trap for 30 ms before switching on the disorder speckle laser. Lastly, the cloud is imaged in situ by absorption imaging. The atom number is determined by summing up the intensity of the picture pixel-wise.

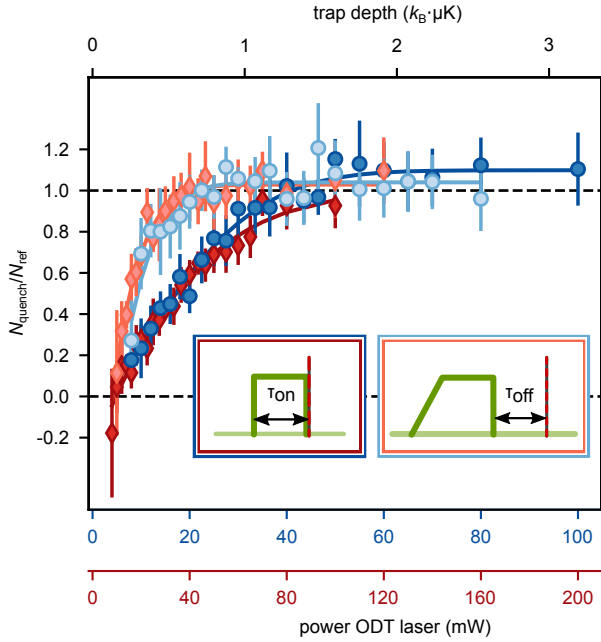


Supplementary Fig. 1. **Comparison of different fit functions to in situ and expansion density profiles.** Measured line density (gray points) in dependence of the x and y direction, once in the mBEC regime at 763.6 G and once at resonance at 832.2 G. (a,b) mBEC, in situ and expansion in dependence of the x direction, fit to the data with a Thomas-Fermi fit in the mBEC regime (solid blue line). (c & d) mBEC, in situ and expansion in dependence of the y direction, fitting to the data with a bimodal fit (solid orange line). The bimodal fit consists of a Thomas-Fermi fit (solid blue line) and a fit with a Gaussian profile (rose dashed-dotted line). (e & f) At unitarity, in situ and expansion in dependence of the x direction, fit to the data with a Thomas-Fermi fit in the mBEC regime (solid blue line) and with one of a UFG (red dashed line). (g & h) At unitarity, in situ and expansion in dependence of the y direction, fit to the data with a bimodal fit (solid orange line). The bimodal fit consists of a Thomas-Fermi fit in the mBEC regime (solid blue line) and a fit with a Gauss profile (rose dashed-dotted line). For comparison, a fit with a Thomas-Fermi fit at resonance (red dashed line). d) & h) show the line densities in y direction by expansion of the cloud. The measured line density is only fitted in the area marked with the green background and the whole cloud is inferred. Due to systematic imaging errors, it is difficult to fit the whole range. At resonance, both fit-methods fit well with the data.

C. Hydrodynamics from quantum to classical regimes

In order to compare the maximum aspect ratio of quantum gases after quenching the disorder potential with that of a gas above the critical temperature, we record the hydrodynamic expansion of a thermal gas without disorder. The temperature of the gas is adjustable via the final laser power of the ODT during evaporation. The power of the ODT laser at the end of the evaporation is varied between 8 mW and 350 mW. Afterward, the trap is compressed by increasing the power of the ODT laser. To avoid further evaporation and have the same conditions for the different powers at the end of the evaporation, the power for the compression is set to 400 mW for all varied powers. At an ODT laser power of 350 mW at the end of evaporation, the atomic cloud has a temperature of about 1200 nK. We measure the maximum aspect ratio of the cloud by expansion for two magnetic field strengths, 763.6 G and 832.2 G (see Supplementary Fig. 3). In both regimes, we see a decrease in the maximum aspect

ratio with increasing power, i.e., temperature until it reaches a final state, a thermal gas, exhibiting purely classical hydrodynamics. At this final state, there is no long-range phase coherence present. For the UFG, the aspect ratio of the final, thermal state is higher than that of the mBEC. We attribute this to stronger interactions, leading to stronger collisional hydrodynamics. Due to the higher ODT power of 400 mW (power for the compression of values in Supplementary Fig. 3) compared to 80 mW (shown in Fig. 2(a) and Fig. 3(c) without losses), the aspect ratios are not comparable since the power effects the trap frequencies. Therefore, the aspect ratio of the thermal gas at 400 mW is adjusted to the one in Fig. 2(a) and Fig. 3(c) at 80 mW. It is scaled according to $\sqrt{\omega_{80\text{ mW}}/\omega_{400\text{ mW}}}$, where ω is the geometric mean of the trap frequencies in the radial directions. This follows from the ideal-gas condensate, where the expansion radius is proportional to the square-root of the trap frequency [58]. In addition, the thermal gas aspect ratio data for both interaction regimes in Fig. 1(d), measured at an ODT laser power of 400 mW, are scaled similarly, since the ideal time evolu-

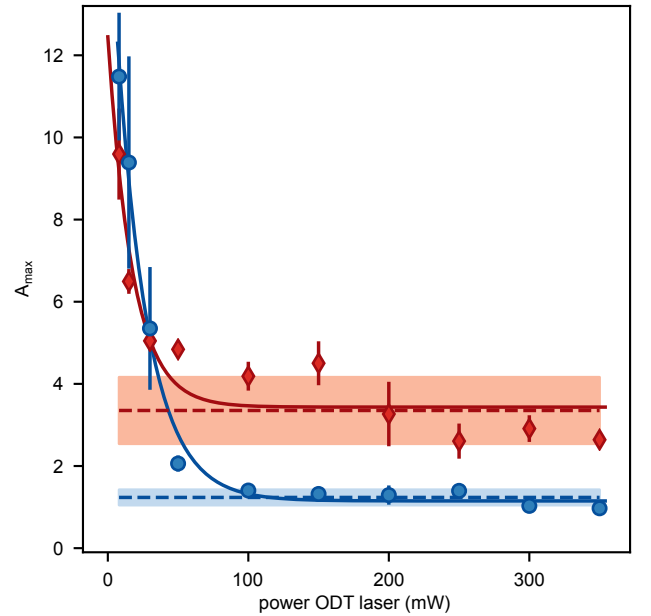


Supplementary Fig. 2. **Mapping losses.** Mapping of remaining atoms $N_{\text{quench}}/N_{\text{ref}}$ in the trap after quenching the disorder field as a function of the power of the ODT laser for the compression. N_{quench} (N_{ref}) is the atom number with (without) disorder field. For the unitary regime (832.2 G), a speckle power of 10 W (red, diamonds) and for the mBEC regime (763.6 G) a speckle power of 5 W is applied (blue, circles). The data points for the decay (dark) and the ones for the revival (light) are shown. The error bars are calculated by the error propagation of the standard deviation of five repetitions. The solid lines are fits with an error function. For comparison, the power of the ODT laser is mapped to the trap depth because this is different for molecules and atoms for the same powers (see red and blue axis). The left (right) inset shows the disorder pulse shape for the decay (revival) of the quantum properties. The imaging (vertical red line in inset) takes place in situ after an expansion time $d = 0$.

tion is computed for 80 mW as for the degenerate regime.

SUPPLEMENTARY NOTE 2: DENSITY RESPONSE TO DISORDER QUENCHES

The disorder potential leads to a spatial density variation of the cloud. For every parameter set used to measure the hydrodynamic response of quantum gases, we have also measured the density response. The difference between probing the density or the hydrodynamic response is the expansion time d . The density variation is probed by in-situ ($d = 0$ ms) absorption images of the column-integrated density distribution $n(x, y)$ of the atomic cloud while for probing the hydrodynamic response the expansion time is in the order of $d = 10$ ms. The evaluation procedure of the absorption images is taken from [17]. To extract the disorder-induced per-



Supplementary Fig. 3. **Expansion of a thermal gas.** Maximum aspect ratio A_{max} as a function of the power of the ODT laser at the end of the evaporation. Shown are experimental data of an mBEC at 763.6 G (blue) and a UFG at 832.2 G (red). The experimental data are fitted with an exponential decay function (solid lines). The final state is fitted with a constant (dashed line) by the last six measured values. The fit uncertainties are the blue and red-filled areas around the dashed lines.

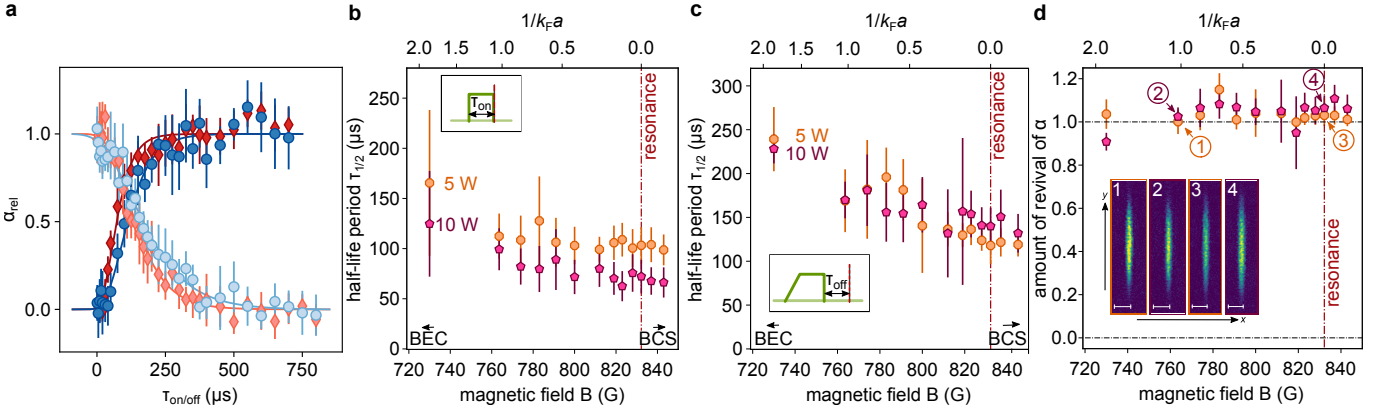
turbation of the cloud, we first fit a 2D Thomas-Fermi profile [58]

$$n_{2D} \propto \left(1 - \frac{(x - x_0)^2}{r_y^2} - \frac{(y - y_0)^2}{r_x^2} \right)^{3/2}, \quad (\text{S4})$$

which is valid in the mBEC regime. For a UFG, the profile should be distinguished from an mBEC in its power law. However, as discussed in the case of hydrodynamic expansion above, we apply the evaluation described for the mBEC regime for all data in order to obtain a homogeneous analysis. The fitted smooth 2D Thomas-Fermi profile is subtracted from the measured data, leaving only the density variations around the mean. The density perturbation is quantified via the fragmentation α , see Ref. [17], defined as

$$\alpha = \sqrt{\langle \Delta n^2 \rangle - \langle \Delta n \rangle^2}, \quad (\text{S5})$$

with $\Delta = n - n_{\text{fit}}$, where n_{fit} is the fitted 2D Thomas-Fermi profile of the measured density distribution n . Further, the brackets denote averaging over all pixels, where $n_{\text{fit}} > 0$. Due to fluctuations already without any disorder field $\alpha \neq 0$ [17]. In contrast to the hydrodynamic expansion, the fragmentation occurs and recovers on similar time scales. Moreover, the density distribution becomes completely smooth, i.e. fragmentation completely vanishes after disturbing the cloud (see Supplementary Fig.



Supplementary Fig. 4. **Density response to disorder quenches.** (a) Decay (dark blue and dark red) and revival (light blue and light red) of the fragmentation α , normalized to the respective maximum of the fit function (α_{rel}), as a function of the disorder pulse duration τ_{on} or the revival time τ_{off} . Shown are the experimental values of an mBEC at 763.6 G (blue points) and a UFG at 832.2 G (red diamonds), where each data point is averaged from five measurements, and its standard deviation corresponds to the error bar. The solid lines are fits with a Gompertz function. Further, the offset o , which is extracted from the fit, is subtracted from the data and the fit to obtain the fragmentation, which is only caused by the disorder field. (b) Interaction dependence of the density response to quenches into disorder. Half-life period $\tau_{1/2}$ as a function of the magnetic field. As for the expansion dynamics, the half-life period decreases from the mBEC side towards the resonance. The inset shows the pulse shape for the decay measurement. The cloud is immediately imaged in situ after the disorder pulse (vertical red line). Error bars are determined via the fit uncertainties (see Eq.S7). (c) Interaction dependence of the density response to quenches out of disorder. Half-life period $\tau_{1/2}$ as a function of the magnetic field. The half-time period of the density variation decreases with decreasing the interaction parameter. The inset shows the pulse shape for the revival measurement. The cloud is imaged in situ (vertical red line) after the revival time τ_{off} . (d) Amount of revival of the fragmentation α in dependence of the magnetic field B . The fragmentation fully recovers for 5 W (orange) and even for 10 W (purple) power of the disorder laser. The inset shows in situ absorption pictures when the fragmentation reaches its highest value due to the disorder field.

4(a)). This is independent of the interaction strength, the powers of the laser (5 W and 10 W), which creates the disorder potential, and even in an open system with significant atom/molecule losses (see Supplementary Fig. 4 (d) and 5(d)). We interpret this as a consequence of local transport processes occurring, where we cannot distinguish classical or quantum contributions. For extracting the half-life period, the fragmentation is fitted with a Gompertz function g [17, 59]

$$g(t) = a e^{-e^{-t/c}/b} + o, \quad (\text{S6})$$

with the fit parameters a , b , c and o . The half-life period $\tau_{1/2}$ is calculated by

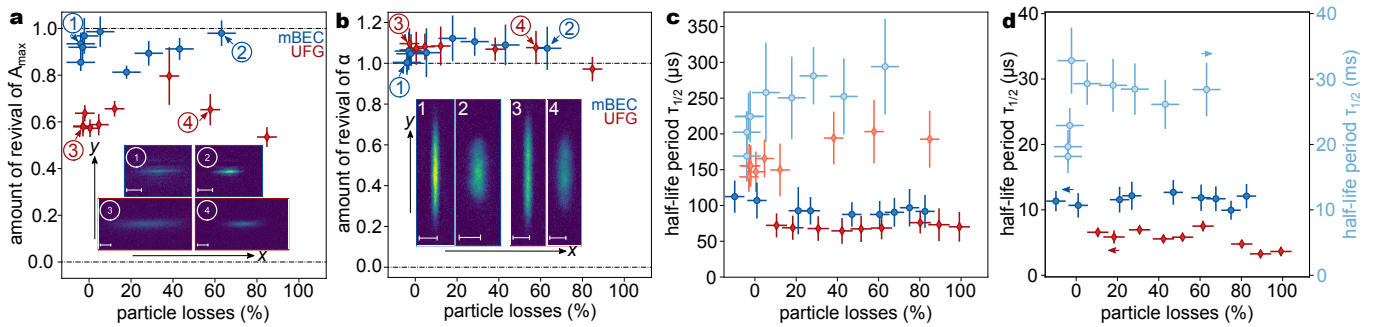
$$\tau_{1/2} = -c \ln(b \ln(2)). \quad (\text{S7})$$

The amount of the revival of the fragmentation is calculated from the fit parameters. The minimal fragmentation α_{min} of the revival (quench out of) is set in relation to the minimal fragmentation of the decay measurements (quench into). For the decay measurement, the Gompertz function is calculated for $t = 0$ ($\alpha_{\text{min}} = a e^{(-1/b)} + o$). For the revival measurement, t is considered in the limiting case towards infinity ($\alpha_{\text{min}} = a + o$).

In a direct comparison of the half-life periods between an mBEC and a UFG, we measure that the new final state, for the decay measurement, is assumed faster for a UFG

(UFG: $\tau_{1/2}^{\text{on}} = (72 \pm 17) \mu\text{s}$, mBEC: $\tau_{1/2}^{\text{on}} = (112 \pm 23) \mu\text{s}$). We attribute this to a larger interaction strength and, thus, increased collision rate. The same can also be seen with the revival (UFG: $\tau_{1/2}^{\text{off}} = (140 \pm 21) \mu\text{s}$, mBEC: $\tau_{1/2}^{\text{off}} = (169 \pm 36) \mu\text{s}$). Over the BEC-BCS crossover, we see a decrease in the half-life period with increasing magnetic field (see Supplementary Figs. 4(b) and (c)). This can be attributed to the larger scattering length, where local particle scattering and transport mechanisms may be enhanced.

By directly comparing the hydrodynamics and the density response, we see that the decay of the hydrodynamics for the mBEC and the UFG is one order of magnitude faster than the density response, as has been seen in Ref. [17]. This can be understood intuitively for the mBEC regime, where the quenched disorder potential imprints a random local phase on the many-body wavefunction. This leads to quick dephasing and decay of long-range coherence. Once local phase differences have been established, this phase difference drives local currents that lead to the emergence of the density variation of fragmentation at a later time. Therefore, the density response is delayed compared to the hydrodynamic decay.



Supplementary Fig. 5. **Quench in an open system.** (a) Amount of revival of the maximum aspect ratio A_{\max} as a function of atom losses (see Methods), which are controlled via the trap depth. An mBEC, blue circles, (UFG, red diamonds) at 763.6 G (832.2 G) is perturbed with 5 W (10 W) disorder laser power. The aspect ratio after a long revival time ($\tau_{\text{off}} > 200$ ms) is taken as the maximum achievable quantum hydrodynamic in equilibrium taken from a fit to eq. (5) as in panel Fig. 3(a) and normalized to the maximum value without disorder, see Methods. The insets show absorption images for the indicated parameters. (b - d) Density response for disorder quenches in an open system. Particle losses for the mBEC (UFG) at 763.6 G (832.2 G) for a power of the disorder laser of 5 W (10 W) (b) Amount of the revival of the fragmentation. The minimum of fragmentation of the revival measurement is set in ratio to the minimum of the fragmentation α_{\min} of the decay measurement. Values are extracted from the fit parameters of the Gompertz-fit, and the error bars are calculated via error propagation of the fit uncertainties. (c) Half-life period $\tau_{1/2}$ for the decay (dark) and revival (bright) of density variation for the unitary (red) and mBEC (blue) regime as a function of provoked atom losses. Revival takes roughly a factor of two longer than the decay of the density. The decay time for expansion and fragmentation is unaffected by losses, but the revival time increases with particle losses. (d) Half-life period $\tau_{1/2}$ for the decay (dark) and revival (bright) of the aspect ratio for a UFG (red) and mBEC (blue) as a function of provoked particle losses. Only the mBEC is shown for the revival because the UFG does not fully revive.

SUPPLEMENTARY NOTE 3: OPEN-SYSTEM DISORDER QUENCHES

Furthermore, we have also studied the response for dissipative quenches (see Supplementary Fig. 5(a-d)). Supplementary Figure 5(a) shows the amount of revival of the aspect ratio as a function of the particle losses that occurred. For the density response, even with losses, the fragmentation fully revives for an mBEC and a UFG (see Supplementary Fig. 5(b)). The losses influence the revival time, which increases for both interaction regimes with higher particle losses (see Supplementary Fig. 5(c)). The half-life period for the decay seems to be unaffected

by the particle losses. This might be explained by a modified density after loss have occurred. The local collisions that re-smooth the density occur at a reduced rate when the density is reduced, resulting in a longer time to reach equilibrium. Further, the same is observed for the half-life period by the hydrodynamic response of the mBEC (see Supplementary Fig. 5(d)). As in [17], the half-life period for the revival of an mBEC takes some orders of magnitude longer than the decay. For reduced density, the time for reaching an equilibrium quantum gas is reduced. We attribute this to the fact that the local collision rate sets the time for decay of Bogoliubov excitations.

-
- [1] C. Chin, R. Grimm, P. Julienne, and E. Tiesinga, Feshbach resonances in ultracold gases, *Rev. Mod. Phys.* **82**, 1225 (2010).
- [2] C. A. R. Sá de Melo, When fermions become bosons: Pairing in ultracold gases, *Physics Today* **61**, 45 (2008).
- [3] W. Zwerger, *The BCS-BEC Crossover and the Unitary Fermi Gas* (Springer, 2012).
- [4] D. E. Miller, J. K. Chin, C. A. Stan, Y. Liu, W. Setiawan, C. Sanner, and W. Ketterle, Critical Velocity for Superfluid Flow across the BEC-BCS Crossover, *Phys. Rev. Lett.* **99**, 070402 (2007).
- [5] W. Weimer, K. Morgener, V. P. Singh, J. Siegl, K. Hueck, N. Luick, L. Mathey, and H. Moritz, Critical Velocity in the BEC-BCS Crossover, *Phys. Rev. Lett.* **114**, 095301 (2015).
- [6] M. Randeria and E. Taylor, Crossover from Bardeen-Cooper-Schrieffer to Bose-Einstein Condensation and the Unitary Fermi Gas, *Annual Review of Condensed Matter Physics* **5**, 209 (2014).
- [7] G. C. Strinati, P. Pieri, G. Röpke, P. Schuck, and M. Urban, The BCS-BEC crossover: From ultra-cold Fermi gases to nuclear systems, *Physics Reports* **738**, 1 (2018).
- [8] G. Shen, C. J. Horowitz, and S. Teige, Equation of state of nuclear matter in a virial expansion of nucleons and nuclei, *Phys. Rev. C* **82**, 045802 (2010).
- [9] J. Carlson, S. Gandolfi, and A. Gezerlis, Quantum Monte Carlo approaches to nuclear and atomic physics, *Progress of Theoretical and Experimental Physics* **2012**, 01A209 (2012).
- [10] A. Gezerlis and J. Carlson, Strongly paired fermions: Cold atoms and neutron matter, *Phys. Rev. C* **77**, 032801 (2008).

- (2008).
- [11] J. R. Engelbrecht, M. Randeria, and C. A. R. Sá de Melo, BCS to Bose crossover: Broken-symmetry state, *Phys. Rev. B* **55**, 15153 (1997).
- [12] C. A. R. Sá de Melo, M. Randeria, and J. R. Engelbrecht, Crossover from BCS to Bose superconductivity: Transition temperature and time-dependent Ginzburg-Landau theory, *Phys. Rev. Lett.* **71**, 3202 (1993).
- [13] C. H. Schunck, Y. Shin, A. Schirotzek, and W. Ketterle, Determination of the fermion pair size in a resonantly interacting superfluid, *Nature* **454**, 739 (2008).
- [14] H. Biss, L. Sobirey, N. Luick, M. Bohlen, J. J. Kinnunen, G. M. Bruun, T. Lompe, and H. Moritz, Excitation Spectrum and Superfluid Gap of an Ultracold Fermi Gas, *Phys. Rev. Lett.* **128**, 100401 (2022).
- [15] S. Hoinka, P. Dyke, M. G. Lingham, J. J. Kinnunen, G. M. Bruun, and C. J. Vale, Goldstone mode and pair-breaking excitations in atomic Fermi superfluids, *Nature Physics* **13**, 943 (2017).
- [16] C. Chin, M. Bartenstein, A. Altmeyer, S. Riedl, S. Jochim, J. H. Denschlag, and R. Grimm, Observation of the Pairing Gap in a Strongly Interacting Fermi Gas, *Science* **305**, 1128 (2004).
- [17] B. Nagler, S. Barbosa, J. Koch, G. Orso, and A. Widera, Observing the loss and revival of long-range phase coherence through disorder quenches, *Proceedings of the National Academy of Sciences* **119**, e2111078118 (2022).
- [18] P. Anderson, Theory of dirty superconductors, *Journal of Physics and Chemistry of Solids* **11**, 26 (1959).
- [19] L. Han and C. A. R. Sá de Melo, Evolution from Bardeen–Cooper–Schrieffer to Bose–Einstein condensate superfluidity in the presence of disorder, *New Journal of Physics* **13**, 055012 (2011).
- [20] G. Orso, BCS-BEC Crossover in a Random External Potential, *Phys. Rev. Lett.* **99**, 250402 (2007).
- [21] A. Khan, S. Basu, and S. W. Kim, Effect of disorder in BCS–BEC crossover, *Journal of Physics B: Atomic, Molecular and Optical Physics* **45**, 135302 (2012).
- [22] F. Palestini and G. C. Strinati, Systematic investigation of the effects of disorder at the lowest order throughout the BCS-BEC crossover, *Phys. Rev. B* **88**, 174504 (2013).
- [23] A. Joshi and P. Majumdar, Impact of speckle disorder on a superfluid Fermi system, *Phys. Rev. B* **100**, 045149 (2019).
- [24] B. Nagler, M. Radonjić, S. Barbosa, J. Koch, A. Pester, and A. Widera, Cloud shape of a molecular Bose–Einstein condensate in a disordered trap: a case study of the dirty boson problem, *New Journal of Physics* **22**, 033021 (2020).
- [25] S. Krinner, D. Stadler, J. Meineke, J.-P. Brantut, and T. Esslinger, Observation of a Fragmented, Strongly Interacting Fermi Gas, *Phys. Rev. Lett.* **115**, 045302 (2015).
- [26] S. Krinner, D. Stadler, J. Meineke, J.-P. Brantut, and T. Esslinger, Superfluidity with disorder in a thin film of quantum gas, *Phys. Rev. Lett.* **110**, 100601 (2013).
- [27] B. Nagler, K. Jägering, A. Sheikhan, S. Barbosa, J. Koch, S. Eggert, I. Schneider, and A. Widera, Dipole oscillations of fermionic quantum gases along the BEC-BCS crossover in disordered potentials, *Phys. Rev. A* **101**, 053633 (2020).
- [28] G. Zürn, T. Lompe, A. N. Wenz, S. Jochim, P. S. Julienne, and J. M. Hutson, Precise Characterization of ^6Li Feshbach Resonances Using Trap-Sideband-Resolved RF Spectroscopy of Weakly Bound Molecules, *Phys. Rev. Lett.* **110**, 135301 (2013).
- [29] Q. Chen, J. Stajic, and K. Levin, Thermodynamics of Interacting Fermions in Atomic Traps, *Phys. Rev. Lett.* **95**, 260405 (2005).
- [30] L. C. M. Ku, A. Sommer and M. Zwierlein, Revealing the Superfluid Lambda Transition in the Universal Thermodynamics of a Unitary Fermi Gas, *Science* **335**, 563 (2012).
- [31] K. M. O’Hara, S. L. Hemmer, M. E. Gehm, S. R. Granade, and J. E. Thomas, Observation of a Strongly Interacting Degenerate Fermi Gas of Atoms, *Science* **298**, 2179 (2002).
- [32] C. Cao, E. Elliott, J. Joseph, H. Wu, J. Petricka, T. Schäfer, and J. E. Thomas, Universal Quantum Viscosity in a Unitary Fermi Gas, *Science* **331**, 58 (2011).
- [33] M. J. Wright, S. Riedl, A. Altmeyer, C. Kohstall, E. R. S. Guajardo, J. H. Denschlag, and R. Grimm, Finite-Temperature Collective Dynamics of a Fermi Gas in the BEC-BCS Crossover, *Phys. Rev. Lett.* **99**, 150403 (2007).
- [34] S. Giorgini, L. P. Pitaevskii, and S. Stringari, Theory of ultracold atomic Fermi gases, *Rev. Mod. Phys.* **80**, 1215 (2008).
- [35] B. Gänger, J. Phieler, B. Nagler, and A. Widera, A versatile apparatus for fermionic lithium quantum gases based on an interference-filter laser system, *Rev. Sci. Instrum.* **89**, 093105 (2018).
- [36] B. Gänger, *Towards a degenerate Fermi gas in a disordered environment*, Ph.D. thesis, University of Kaiserslautern, Supervisor: Artur Widera (2019).
- [37] S. Jochim, M. Bartenstein, A. Altmeyer, G. Hendl, C. Chin, J. H. Denschlag, and R. Grimm, Pure Gas of Optically Trapped Molecules Created from Fermionic Atoms, *Phys. Rev. Lett.* **91**, 240402 (2003).
- [38] G. Valtolina, A. Burchianti, A. Amico, E. Neri, K. Khani, J. Seman, A. Trobettoni, A. Smerzi, M. Zaccanti, M. Inguscio, and G. Roati, Josephson effect in fermionic superfluids across the BEC-BCS crossover, *Science* **350**, 1505 (2015).
- [39] W. Kwon, D. P. G., P. R., M. Inguscio, W. Zwerger, M. Zaccanti, S. F., and G. Roati, Strongly correlated superfluid order parameters from dc Josephson supercurrents, *Science* **369**, 84 (2020).
- [40] B. Shapiro, Cold atoms in the presence of disorder, *Journal of Physics A: Mathematical and Theoretical* **45**, 143001 (2012).
- [41] B. Nagler, M. Will, S. Hiebel, S. Barbosa, J. Koch, M. Fleischhauer, and A. Widera, Ultracold Bose Gases in Dynamic Disorder with Tunable Correlation Time, *Phys. Rev. Lett.* **128**, 233601 (2022).
- [42] S. Hiebel, B. Nagler, S. Barbosa, J. Koch, and A. Widera, Characterizing quantum gases in correlated-disorder realizations using density-density correlations, *arXiv* <https://doi.org/10.48550/arXiv.2306.16099> (2023).
- [43] A. V. Lopatin and V. M. Vinokur, Thermodynamics of the Superfluid Dilute Bose Gas with Disorder, *Phys. Rev. Lett.* **88**, 235503 (2002).
- [44] R. Grimm, Ultracold Fermi gases in the BEC-BCS crossover: a review from the Innsbruck perspective, *arXiv* <https://doi.org/10.48550/arXiv.cond-mat/0703091> (2007).
- [45] M. Marini, F. Pistolesi, and G. Strinati, Evolution from BCS superconductivity to Bose condensation: analytic results for the crossover in three dimensions, *Eur. Phys.*

- J. B **1**, 151 (1998).
- [46] F. Pistolesi and G. C. Strinati, Evolution from BCS superconductivity to Bose condensation: Calculation of the zero-temperature phase coherence length, *Phys. Rev. B* **53**, 15168 (1996).
- [47] F. Pistolesi and G. C. Strinati, Evolution from BCS superconductivity to Bose condensation: Role of the parameter $k_F \xi$, *Phys. Rev. B* **49**, 6356 (1994).
- [48] D. Delande and G. Orso, Mobility Edge for Cold Atoms in Laser Speckle Potentials, *Phys. Rev. Lett.* **113**, 060601 (2014).
- [49] A. Ghosal, M. Randeria, and N. Trivedi, Inhomogeneous pairing in highly disordered s-wave superconductors, *Phys. Rev. B* **65**, 014501 (2001).
- [50] B. Nagler, *Bose-Einstein condensates and degenerate Fermi gases in static and dynamic disorder potentials*, Ph.D. thesis, University of Kaiserslautern, Supervisor: Artur Widera (2020).
- [51] L. Pitaevskii and S. Stringari, *Bose-Einstein Condensation and Superfluidity* (Oxford University Press, 2016).
- [52] D. S. Petrov, C. Salomon, and G. V. Shlyapnikov, Weakly Bound Dimers of Fermionic Atoms, *Phys. Rev. Lett.* **93**, 090404 (2004).
- [53] J. Kinast, A. Turlapov, J. E. Thomas, Q. Chen, J. Stajic, and K. Levin, Heat Capacity of a Strongly Interacting Fermi Gas, *Science* **307**, 1296 (2005).
- [54] M. W. Z. Wolfgang Ketterle, Making, probing and understanding ultracold Fermi gases, arXiv <https://doi.org/10.1393/ncr/i2008-10033-1> (2008).
- [55] J. Koch, S. Barbosa, F. Lang, and A. Widera, Stability and sensitivity of interacting fermionic superfluids to quenched disorder [Data set], Zenodo DOI: 10.5281/zenodo.13292670 (2024).
- [56] S. Jochim, *Bose-Einstein Condensation of Molecules*, Ph.D. thesis, Leopold-Franzens-Universität Innsbruck, Supervisor: Rudolf Grimm (2004).
- [57] M. Bartenstein, A. Altmeyer, S. Riedl, S. Jochim, C. Chin, J. H. Denschlag, and R. Grimm, Crossover from a Molecular Bose-Einstein Condensate to a Degenerate Fermi Gas, *Phys. Rev. Lett.* **92**, 120401 (2004).
- [58] D. S.-K. W. Ketterle, D.S. Durfee, Making, probing and understanding Bose-Einstein condensates, arXiv <https://doi.org/10.48550/arXiv.cond-mat/9904034> (1999).
- [59] E. W. Weisstein, "Gompertz Curve." From MathWorld—A Wolfram Web Resource (accessed: 05.06.2023), <https://mathworld.wolfram.com/GompertzCurve.html>.